PCCP

Accepted Manuscript

ROYAL SOCIETY OF CHEMISTRY

www.rsc.org/pccp

PCCP

RSCPublishing

ARTICLE

Cite this: DOI: 10.1039/x0xx00000x

Received 00th January 2014,
Accepted 00th January 2014

DOI: 10.1039/x0xx00000x

www.rsc.org/

Mn concentration-dependent tuning of Mn^{2+} d emission of $Zn_{1-x}Mn_xTe$ nanocrystals grown in a glass system

Alessandra S. Silva*[a], Sidney A. Lourenço[b], Noelio O. Dantas[a]

We studied the effect of Mn concentration on the optical, morphological and magnetic properties of $Zn_{1-x}Mn_xTe$ NCs grown in a glass matrix produced by the fusion method. The physical properties of these materials were determined by optical absorption (OA), transmission electron microscopy (TEM), atomic/magnetic force microscopy (AFM/MFM) and photoluminescence (PL). An analysis of the OA spectra, based on the crystal field theory (CFT), showed strong evidence that Mn^{2+} ions were substitutionally incorporated into the $Zn_{1-x}Mn_xTe$ NCs until reaching the solubility limit (concentration, x = 0.100). Above this nominal concentration, TEM showed the onset of Mn-related phases, such as MnO and α-MnO_2, in the PZABP glass system. AFM images showed that NC density on the surface of the glass matrix decreased as x-content increased. It is probable that MnO and MnO_2 NCs would outnumber $Zn_{1-x}Mn_xTe$ NCs at higher concentrations - a conclusion that was corroborated by the OA spectra and TEM images. MFM images revealed that samples with Mn^{2+} ions responded to magnetization from an MFM probe. This implied that Mn^{2+} ions were incorporated within the $Zn_{1-x}Mn_xTe$ NCs and gave rise to the diluted magnetic semiconductor (DMS) structure.The PL spectra not only confirmed the evidence obtained by OA, CFT, TEM and AFM/MFM, but also showed that Mn^{2+} concentration could be used to tune $^4T_1(^4G) \rightarrow {}^6A_1(^6S)$ emission energy.

1. Introduction

$Zn_{1-x}Mn_xTe$ nanocrystals (NCs) of quantum confinement size belong to the diluted magnetic semiconductor (DMS) quantum dot (QD) class of materials that has been widely studied in recent years due to its potential in spintronic and nanomagnetic applications.[1-3] Incorporating transition metal ions in DMS creates intermediate energy states between the valence and conduction bands of the host semiconductor and allows manipulation of the host's magnetic-optical properties,[4] which in turn governs *sp-d* spin interaction between carriers and magnetic ions.[5,6] For example, Mn^{2+} ions that are incorporated into quantum-confined NC semiconductors can act as recombination centers for excited electron-hole pairs, thereby producing the characteristic $^4T_1(^4G) \rightarrow {}^6A_1(^6S)$ emission and allowing greater quantum efficiency relative to undoped semiconductors.[7] Thus, one of the main motivations for studying semiconductors doped with transition metals, especially Mn^{2+} ions, is the production of luminescent devices.[8]

The characteristic *d* emission from Mn^{2+} ions incorporated into CdS NCs can, for example, be tuned to 40 nm, which differs from what can be expected for semi-located *d-d* transitions.[9] Surprisingly, this tuning was achieved by finely adjusting the host NC size, which in turn changed the global emission color from red to yellow as NC diameter increased. $^4T_1(^4G) \rightarrow {}^6A_1(^6S)$ emission energy can be tuned by incorporating Mn^{2+} at various NC sites (e.g. nucleus, sub-surface and surface), which produces variations in size and various consequent emissions.[9] This in turn significantly changes the crystal field around the Mn^{2+} ion and, consequently, its local electron structure.

We studied the effect of Mn concentration on the optical, morphological and magnetic properties of $Zn_{1-x}Mn_xTe$ NCs grown in a glass matrix by the fusion method with subsequent thermal annealing. We also used Tanabe-Sugano energy diagrams to determine how higher Mn concentrations (from x = 0.000 to x = 0.800) modify the local crystal field of this transition metal and, consequently, tune the $^4T_1(^4G) \rightarrow {}^6A_1(^6S)$ emission energy of the Mn^{2+} ions incorporated within the $Zn_{1-x}Mn_xTe$ NCs. These physical properties were

investigated by optical absorption (OA), transmission electron microscopy (TEM), atomic/magnetic force microscopy (AFM/MFM) and photoluminescence (PL). To our knowledge, the present study is the first to examine this variation in the local crystal field due to increasing Mn concentration in DMS NCs.

2. Samples and experimental details

$Zn_{1-x}Mn_xTe$ NCs were grown in a PZABP glass matrix (nominal composition: $65P_2O_5{\cdot}14ZnO{\cdot}\ 1Al_2O_3{\cdot}10BaO{\cdot}10PbO$, mol %) by adding 2Te (wt %) and Mn at doping concentration *x* relative to Zn concentration (0 - 80 wt %) and synthesizing by the fusion method. The fusion method consists of two sequential melting-nucleation processes that produce ensembles of nearly spherical nanoparticles embedded in a glass matrix.[10,11] The first step of sample preparation involved melting powder mixtures of the precursor materials at 1300°C for 30 minutes in an alumina crucible and in an appropriate reducing atmosphere. This last step is fundamental since it reduces oxidation of the glass matrix precursors. This reduction further increases the concentration of available Zn^{2+}, Te^{2-} and Mn^{2+} ions, which is necessary for the formation and growth of $Zn_{1-x}Mn_xTe$ NCs. Next, these mixtures were quickly cooled to room temperature forming a glass system doped with the precursor ions needed for nanoparticle growth. Afterwards, the glass samples were thermally annealed at 500 °C for 10 hours to enhance the diffusion of Zn^{2+}, Mn^{2+}, and Te^{2-} ions throughout the host PZABP matrix and induce growth of $Zn_{1-x}Mn_xTe$ NCs.

The physical properties of the PZABP glass matrix containing $Zn_{1-x}Mn_xTe$ NCs were studied by optical absorption (OA), transmission electron microscopy (TEM), atomic/magnetic force microscopy (AFM/MFM) and Photoluminescence (PL). Room temperature OA spectra showed optical transition peaks in the UV-VIS-NIR range from 250 – 750 nm. These peaks were recorded with a model UV-3600 Shimadzu UV-VIS-NIR spectrometer operating between 190 – 3300 nm and at a resolution of 1 nm. NC formation, NC size, and the distance (d) between adjacent lattice planes were investigated using scanning transmission electron micrographs (TEM JOEL, JEM-2100, 200 kV). ImageJ software was used to analyse d-spacing. AFM/MFM images were obtained using a Shimadzu Scanning Probe Microscope (SPM-9600) with a vertical resolution of 0.01 nm. The average radius of the $Zn_{1-x}Mn_xTe$ NCs was determined by analysing the AFM images with GetData Graph Digitizer software and an analysis of fit of the height distributions using a Log-Normal function. Photoluminescence (PL) measurements were taken with a 405 nm (~ 3.06 eV) continuous wave laser focused to a ~ 200 μm ray with an excitation power of 2.5 mW. All measurements were taken at room temperature (300 K).

3. Result and Discussion

Figure 1 shows the OA spectra of the PZABP glass matrix containing $Zn_{1-x}Mn_xTe$ NCs with concentrations (x) varying from 0.000 to 0.800, for 2.0Te (wt %) ($Zn_{1-x}Mn_xTe$ samples) and doped with only 80Mn (wt % of Zn) for comparison (PZABP: 0.8Mn sample). As we have shown in previous studies,[10,11] the OA data demonstrate that the PZABP glass matrix is transparent in the near ultraviolet (UV) range where $Zn_{1-x}Mn_xTe$ NCs exhibit absorption and emission transitions. Therefore, OA spectra are suitable for investigating the growth of $Zn_{1-x}Mn_xTe$ NCs within the PZABP glass matrix used in this study. Figure 1 shows absorption bands centred at approximately 3.09 eV (400 nm) and 2.33 eV (535 nm) ($0.000 \leq x \leq 0.050$) that are attributed to $Zn_{1-x}Mn_xTe$ nanocrystals in quantum confinement regime (QDs) and with bulk-like properties, respectively.[10,11]

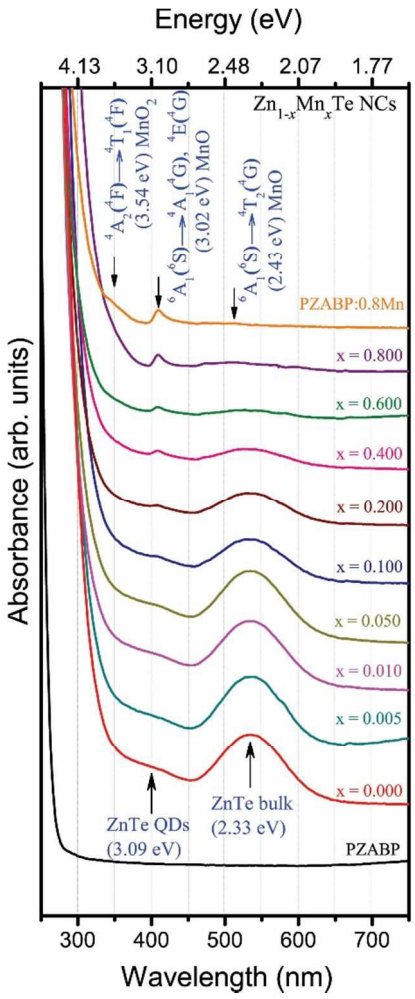

Figure 1. OA spectra of the PZABP template and of $Zn_{1-x}Mn_xTe$ NC samples embedded in this template at different Mn-doping concentrations, ranging from 0.000 to 0.800.

In addition to the absorption bands attributed to $Zn_{1-x}Mn_xTe$ NCs (QDs and NC bulk-like), Figure 1 also shows three additional bands at approximately 350 nm (3.54 eV), 410 nm (3.02 eV) and 510 nm (2.43 eV), ($x \geq 0.100$). These bands increase in intensity from x = 0.100 to x = 0.800 and also appear when the PZABP matrix is doped with only Mn (PZABP:0.8Mn sample). The absorption band centred at 350 nm can be attributed to the $^4A_2(^4F) \rightarrow {}^4T_1(^4F)$ transition from Mn^{4+} ($3d^3$) ions that are probably located at NC sites in MnO_2.[12] The bands centred at 410 nm and 510 nm can be attributed, respectively to $^6A_1(^6S) \rightarrow {}^4A_1(^4G),{}^4E(^4G)$ and $^6A_1(^6S)$

$\rightarrow {}^4T_2({}^4G)$ de $Mn^{2+}(3d^5)$ transitions[13] that are probably located at NC sites in MnO. Additionally, as *x*-content increases beyond $x = 0.100$, the optical density of the $Zn_{1-x}Mn_xTe$ NCs (QDs and bulk-like) decreases. At higher Mn concentrations, the nucleation rate for forming MnO and MnO_2 NCs probably surpasses that of $Zn_{1-x}Mn_xTe$ NCs, and in turn inhibits the formation of $Zn_{1-x}Mn_xTe$ NCs. Thus, the OA spectra show that there are more MnO and MnO_2 NCs than $Zn_{1-x}Mn_xTe$ NCs at high concentrations.

Application of the crystal field theory (CFT) in this context is appropriate because it uses OA spectra (Fig. 1) to calculate crystal field strength Δ and the Racah B parameter that considers both the tetrahedral and octahedral electronic configuration of Mn^{2+} ($3d^5$) and Mn^{4+} ($3d^3$). According to CFT, the ${}^6S$ ground state in the $3d^5$ electronic configuration of Mn^{2+} divides into two states (${}^6A_1$ - weak field and ${}^2T_2$ - strong field) while the ${}^4G$ excited state separates into three states (${}^4A_1$,${}^4E(G)$, ${}^4T_2$ and ${}^4T_1$) (Fig. 2 (B)). Furthermore, the ${}^4F$ ground state of Mn^{4+} divides into three states (${}^4T_1$, ${}^4T_2$ and ${}^4A_2$) while the ${}^2G$ excited state divides into four sates (${}^2A_1$, ${}^2T_2$, ${}^2T_1$ and ${}^2E$) (Fig. 2 (A)) as shown in the Tanabe-Sugano diagrams with C/B = 4.50.[14] Thus, by using the CFT and experimental optical date, the energy of the ${}^6A_1({}^6S) \rightarrow {}^4A_1({}^4G)$,${}^4E({}^4G)$ and ${}^6A_1({}^6S) \rightarrow {}^4T_2({}^4G)$ transitions of Mn^{2+} ($3d^5$) ions can be effectively described by the Racah B parameter (762.19 cm^{-1}) and crystal-field splitting (Δ = 12957.23 cm^{-1}), as represented by the solid vertical line at Δ/B = 17. The energy corresponding to the ${}^4A_2({}^4F) \rightarrow {}^4T_1({}^4F)$ transition in Mn^{4+} ($3d^3$) ions is effectively described by B = 1068.35 cm^{-1}, Δ = 19230.23 cm^{-1} and Δ/B = 18. Figure 2 (C) shows the OA spectra of the glass samples containing $Zn_{1-x}Mn_xTe$ NCs with x = 0.80 ($Zn_{0.2}Mn_{0.8}Te$) and the PZABP glass matrix doped only with Mn (PZABP: 0.80Mn). Here, dotted lines represent the transitions observed in the Tanabe-Sugano diagrams (Figs. 2 (A) and 2 (B)).

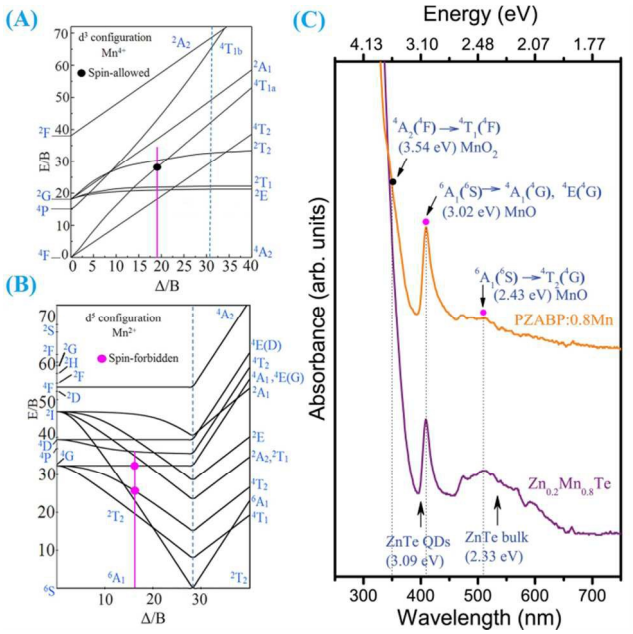

Figure 2. Tanabe-Sugano diagram of (A) d^3 and (B) d^5 for C/B = 4.5. (C) Optical absorption spectra of glass samples containing $Zn_{1-x}Mn_xTe$ NCs with x = 0.800 ($Zn_{0.2}Mn_{0.8}Te$), and of the glass matrix doped only with Mn (PZABP: 0.8Mn). Dotted lines represent the transitions observed in the Tanabe-Sugano diagrams (left side). Experimental Crystal-field energies obtained from the optical spectra are represented by dots at Δ/B = 17 for the Mn^{2+} ($3d^5$) electronic configuration and Δ/B = 18 for the Mn^{4+} ($3d^3$) electronic configuration – both located in the octahedral site (Figures B and A). Spin-allowed and spin-forbidden transitions can also be seen.

Thus, OA spectra and CFT provide strong evidence of the substitutional incorporation of Mn^{2+} ions in $Zn_{1-x}Mn_xTe$ NCs up to their solubility limit (x = 0.100). At higher concentrations (x > 0.100), MnO and MnO_2 NCs probably begin to form within the PZABP glass.

Figure 3 shows TEM images of glass samples containing $Zn_{1-x}Mn_xTe$ NCs at concentrations (A) x = 0.000, (B) x = 0.010, (C) x = 0.100 and (D) x = 0.800. Amplifications are shown to the side of these images. When the samples are not doped with Mn (x = 0.000), the amplified region of the TEM image (Figure 3 (A)) shows that the distance between the adjacent lattice fringes is ~ 0.346 nm. This value is largely consistent with the value found in the literature for (111) d spacing (0.350 nm) and corresponds to ZnTe NCs with zinc-blend (ZB) structure (JCPDF No. 15-0746).[15] However, when the glass samples are doped with Mn concentrations of x = 0.010, x = 0.100 and x = 0.800, NCs ($Zn_{0.99}Mn_{0.01}Te$, $Zn_{0.9}Mn_{0.1}Te$ and $Zn_{0.2}Mn_{0.8}Te$, respectively) form with virtually the same interplanar distance (d ~ 0.347) as that of the ZnTe NCs (x = 0.000) in the ZB structure (Figures 3 (B), 3 (C) and 3 (D)). This suggests that the lattice pattern of the NCs remains unchanged with the incorporation of Mn^{2+} ions.This result is expected since there is little difference between the Zn^{2+} (0.68 Å) and Mn^{2+} (0.75 Å) ionic radii.[16] Furthermore, at high Mn concentrations (x = 0.100 and x = 0.800), the amplified TEM images show the distances between the adjacent lattice fringes to be approximately 0.223 nm and 0.581 nm, which correspond, respectively, to the (2 0 0) plane of MnO with cubic structure (JCPDF No. 07-0230)[17] and to the (2 2 0) plane of α-MnO_2 with tetragonal structure (JCPDF No. 44-0141).[18] This observation fully corroborates the conclusion drawn from the OA spectra data and clearly confirms the formation of $Zn_{1-x}Mn_xTe$ NCs and manganese oxides (MnO and α-MnO_2) in the glass samples at high Mn concentrations (x > 0.100).

Figure 4 shows bi-dimensional AFM/MFM images of the same glass samples shown in Figure 3. Each figure displays a 250 x 250 nm topographical image of the sample (left panel), with the size distributions of the $Zn_{1-x}Mn_xTe$ NCs and a corresponding magnetic phase image (right panel). The mean radii of the $Zn_{1-x}Mn_xTe$ NCs were determined from the mean height of the particles in the topographical images (AFM). It can be seen that NC size remained unchanged as Mn concentration increased. This is expected, given that all samples were synthesized under the same thermodynamic conditions. Indeed, Figures 4 (A) - (D) show that the mean radius of the $Zn_{1-x}Mn_xTe$ NCs is R ≈ 2.23 nm. The mean radius of the bulk-like NCs was determined to be approximately R ≈ 7.32 nm. It is known that ZnTe NCs begin to exhibit bulk properties when R is greater than approximately 5.39 nm.[11] These results agree with those observed by TEM. Thus, the $Zn_{1-x}Mn_xTe$ QDs, with

small mean radii of R ~ 2.23 nm, exhibit strong quantum confinement given that the exciton Bohr radius of bulk NCs is 5.2 nm.[19]

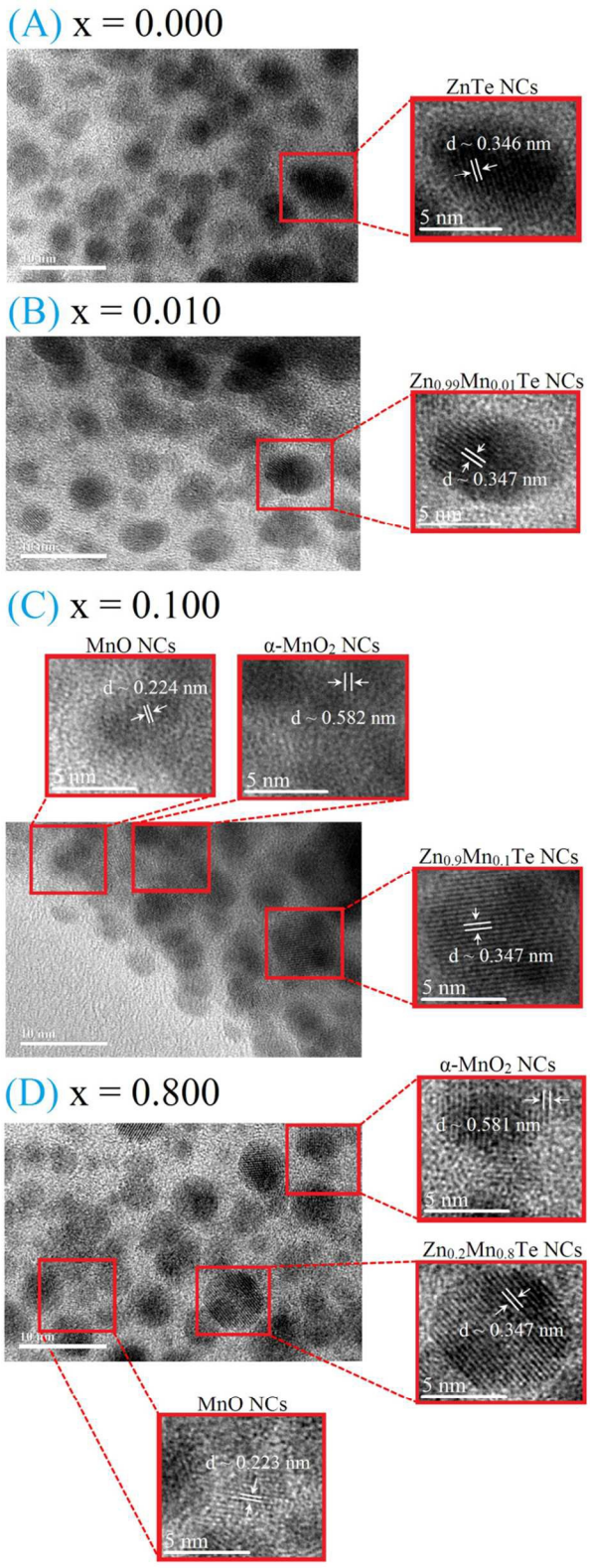

Figure 3. TEM images of the glass samples containing $Zn_{1-x}Mn_xTe$ NCs at concentrations (A) x = 0.000, (B) x = 0.010, (C) x = 0.100 and (D) x = 0.800. The side panels are amplifications of the boxed regions.

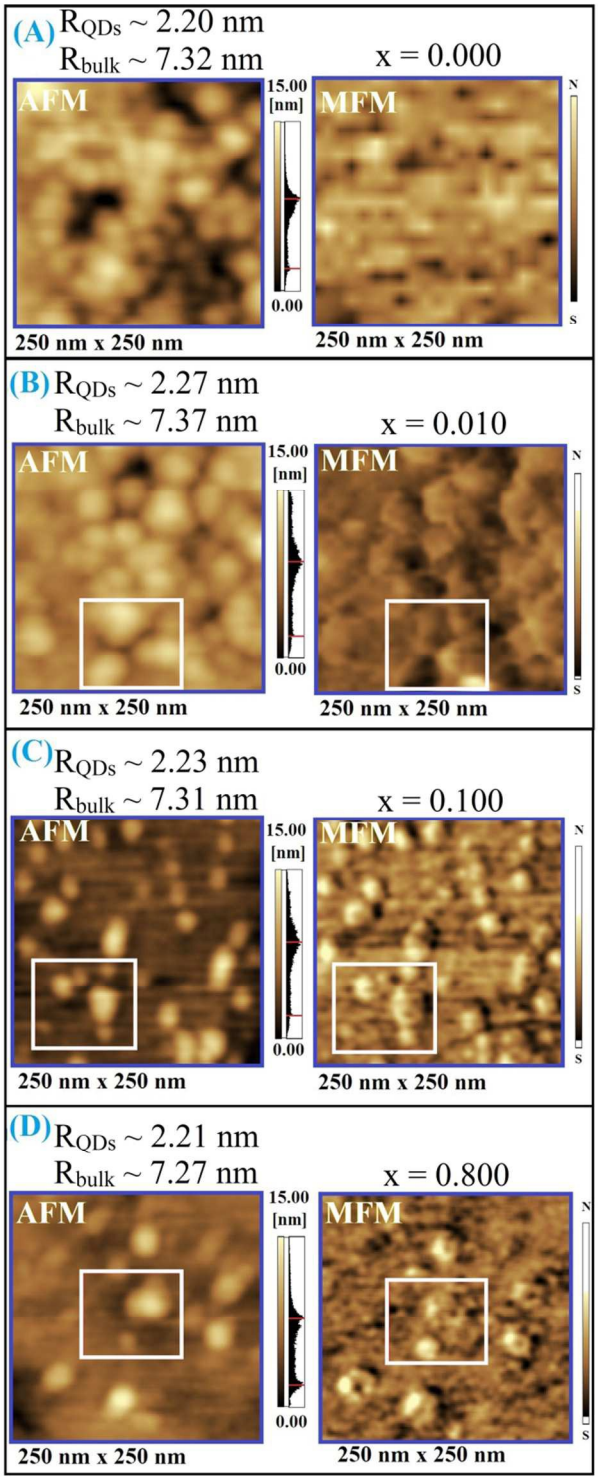

Figure 4. AFM/MFM images of $Zn_{1-x}Mn_xTe$ NCs in the PZABP glass matrix at concentrations (A) x = 0.000, (B) x = 0.010, (C) x = 0.100 and (D) x = 0.800. The left panel shows topographic images (AFM) and the height distributions of the $Zn_{1-x}Mn_xTe$ NCs. The right panel shows the corresponding magnetic phase images (MFM) in which the contrast between the north (N) and south (S) magnetic

poles identifies the orientation of the total magnetic moment of the NCs.

The AFM images also show that NC density on the surface of the glass matrix decreased as x-content increased. This confirms our findings from the OA spectra since the optical density of MnO and MnO_2 NCs (at high concentrations) was lower than that of $Zn_{1-x}Mn_xTe$ (at low concentrations). At high concentrations, MnO and MnO_2 NCs probably outnumbered $Zn_{1-x}Mn_xTe$ NCs.

The magnetic phase images (MFM) in Figures 4 (B) - (D) present contrasts that correspond to magnetic nanocrystalline structures observed in the AFM images (Figure 4, left side). These magnetic contrasts from NCs do not appear as clearly for the undoped sample (x = 0.000), (Figure 4(A)). This difference occurs because the samples containing magnetic ions respond to magnetic stimulus. Thus, the dark (light) contrasts shown in the MFM images, Figs. 4 (B) - (D), indicate that $Zn_{1-x}Mn_xTe$ NCs are magnetic and oriented parallel (antiparallel) to tip magnetization,[10,20] (indicated by the N/S scale bar on the right side of Figs. 4 (A) - (D)). This result provides strong evidence that Mn^{2+} ions were incorporated into the $Zn_{1-x}Mn_xTe$ NCs, forming a DMS structure.[20]

Figure 5 shows photographs (A) and PL spectra (450 to 850 nm) of samples containing $Zn_{1-x}Mn_xTe$ NCs (x = 0.000 to x = 0.800) and the PZABP glass matrix doped only with Mn (wt % of Zn) for comparison (PZABP: 0.8Mn sample) (B). Additionally, Figure 5 (C) shows $Zn_{0.995}Mn_{0.005}Te$ (x = 0.005) with Gaussian fits (C). The photographs are illuminated by white light and show that the PZABP matrix is transparent, whereas the sample doped with $Zn_{1-x}Mn_xTe$ gradually changes colour as concentration increases. However, photographs of the same samples lighted with ultraviolet (UV) light show increasing luminescence at higher manganese ion concentrations. This result indicates that higher concentrations facilitate Mn^{2+} incorporation in $Zn_{1-x}Mn_xTe$ NCs. The PL spectra in Figure 5 (B) (x = 0.000) show emissions from to two groups of NCs of different sizes: an excitonic emission (E_{ex}) from QDs at approximately 500 nm (2.48 eV), an electron-hole recombination (E_b) from bulk-like NCs at approximately 570 nm (2.17 eV) and a third emission at 680 nm (1.82 eV) arising from deep defect levels due to oxygen centres (E_O) in the crystalline structure of the ZnTe NCs.[21,22]

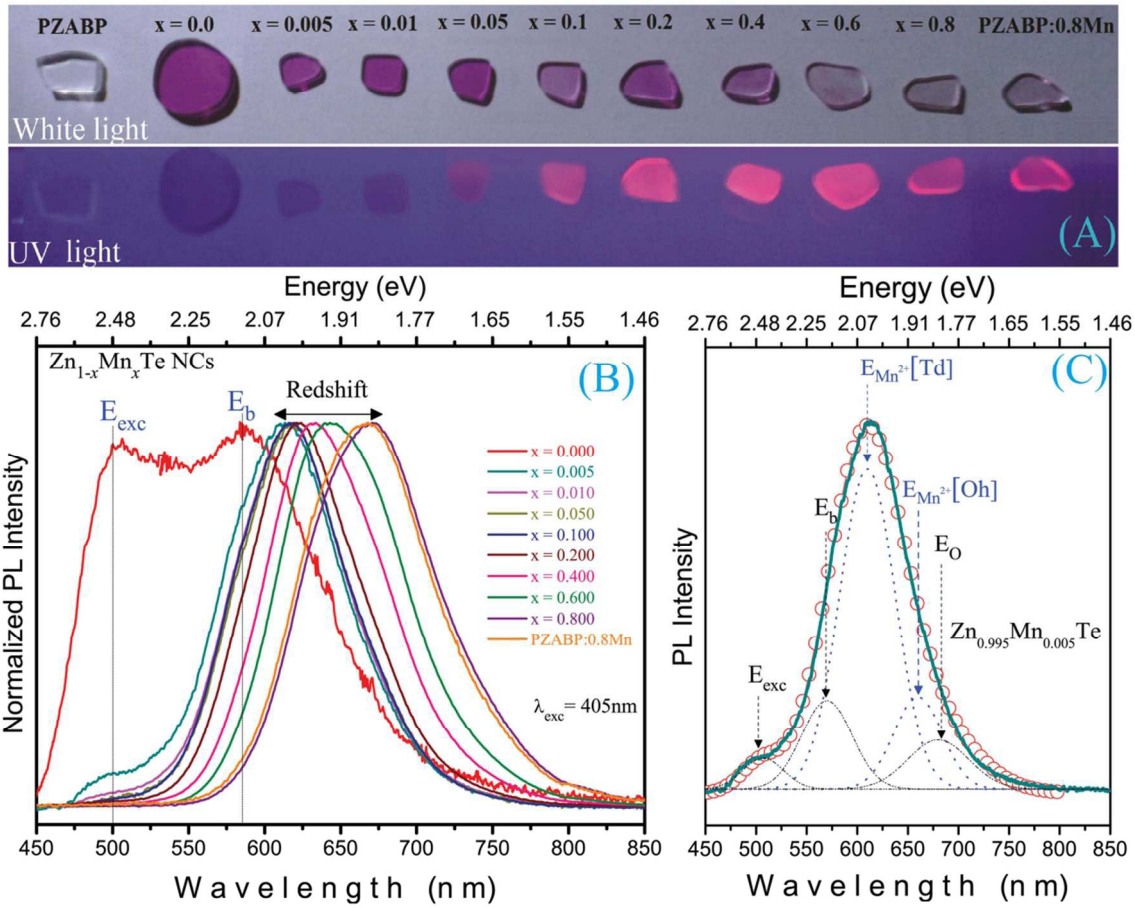

Figure 5. Photographs (A) and PL spectra (B) of the glass samples containing $Zn_{1-x}Mn_xTe$ NCs at concentrations (x) ranging from 0.000 to 0.800. PL spectrum of the glass sample containing $Zn_{0.995}Mn_{0.005}Te$ NCs (x = 0.005) (C). Dashed lines represent the Gaussian component of the experimental data, and the red circles represent the Gaussian fits.

PCCP RSCPublishing

ARTICLE

It is clear that as magnetic doping increased, the substitutional incorporation of Mn^{2+} in $Zn_{1-x}Mn_xTe$ NCs strongly suppressed emissions from QDs (E_{ex}) and bulk-like NCs (E_b). The same result was observed at low Mn concentrations (x = 0.000 a x = 0.050).[10] Samples with $x \neq 0.000$ not only produced these previously mentioned emissions, but also produced a broad band in the PL spectra that redshifted from orange to near infra-red in the electromagnetic spectrum. Typically, d-d transitions are strongly dependent on the ligand field strength of the surrounding ligands because the d-shell is only weakly shielded from its environment (Tanabe-Sugano diagram, Fig. 2(A) and 2(B)). According to the literature, the characteristic luminescent Mn^{2+} ($3d^5$) emission, corresponding to the $^4T_1(^4G) \rightarrow {}^6A_1(^6S)$ transition, consists of a broad band that, depending on its position in the crystal field of the host network, varies from the green electromagnetic spectrum to the red. Green emissions occur when Mn^{2+} is tetrahedrally coordinated (CN = 4) and red when octahedrally coordinated (CN = 6).[23,24] Therefore, the broad band in the PL spectra (Fig. 5(B)) can be attributed to contributions from two transitions of spin-forbidden characteristics of Mn^{2+}: one emission centred at approximately 610 nm (2.03 eV) that corresponds to tetrahedrally coordinated (Td) Mn^{2+} in zinc-blend ZnMnTe NCs and another centred at approximately 660 nm (1.89 eV) that corresponds to octahedrally coordinated (Oh) Mn^{2+} (Fig. 5 (C)) for samples containing $Zn_{0.995}Mn_{0.005}Te$ NCs. The redshift in the PL spectra may be related to a change in the crystal field around the Mn^{2+} ion as Mn concentration increases. This behaviour can also be analysed using the crystal field theory (CFT) that considers the electronic configuration of manganese ions in local symmetries (Figure 6). The Oh coordination of Mn^{2+} (Fig. 5 (C)) may be associated with interstitial doping or growth of the MnO NC.

Figure 6 (A) shows the PL spectra of the glass samples containing $Zn_{1-x}Mn_xTe$ NCs (x = 0.005, 0.100 and 0.800) and Gaussian fits that correspond to the emissions observed in Fig. 5 (C) (x = 0.005) with an additional emission at approximately 715 nm (x = 0.100 and 0.800). Figure 6(B) shows the energy diagrams of Mn^{2+} ($3d^5$) and Mn^{4+} ($3d^3$) with the absorption transitions shown in Fig. 2(C) and the observed emission in Fig. 6(A).

PCCP RSCPublishing

ARTICLE

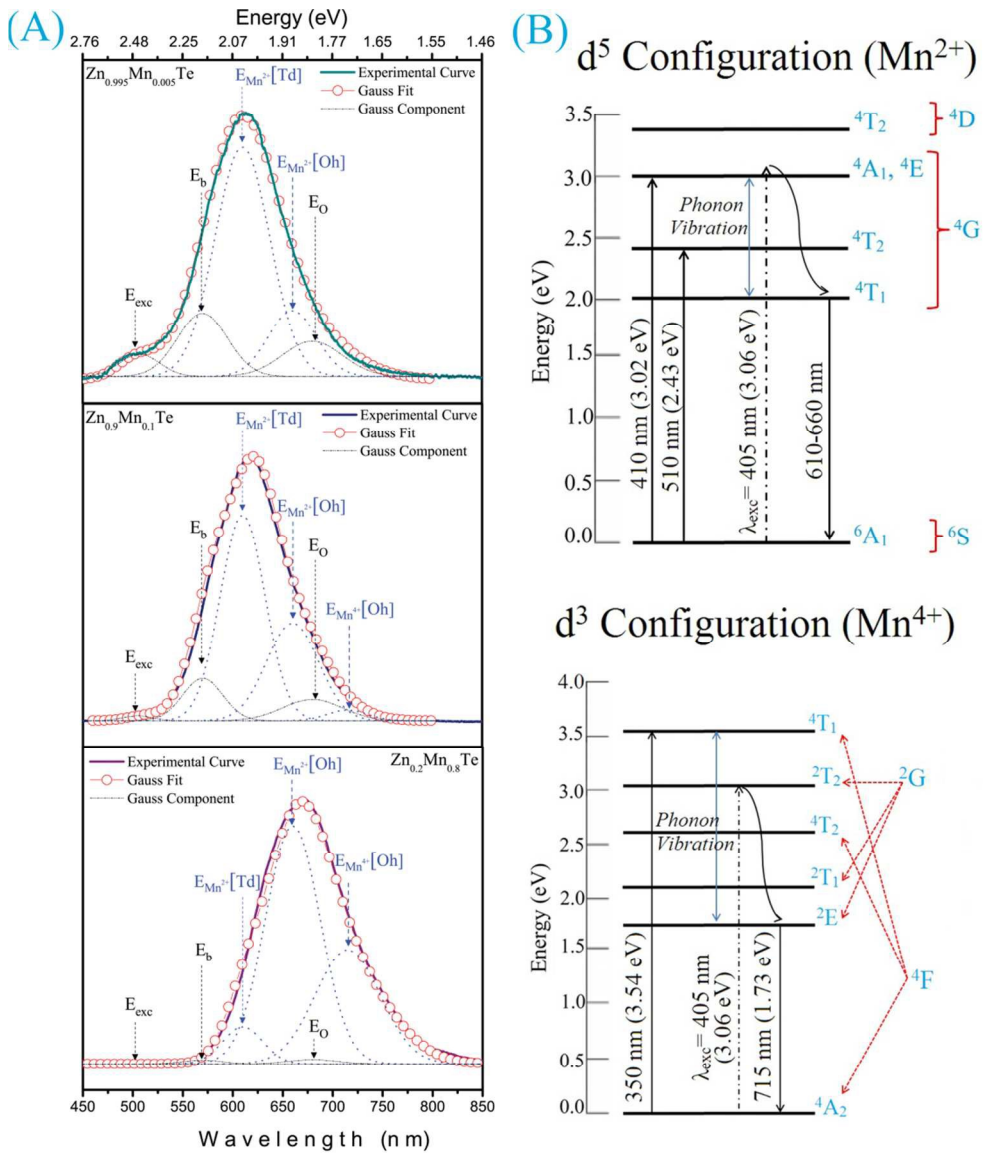

Figure 6. (A) PL spectra of the glass samples containing $Zn_{1-x}Mn_xTe$ NCs, with x = 0.005, 0.100 and 0.800. Dashed lines represent the Gaussian fits of the experimental data. (B) Energy levels of Mn^{2+} ($3d^5$) and Mn^{4+} ($3d^3$) detailed in local symmetries and showing absorption and emission transitions.

The free electrons in the $^6A_1(^6S)$ ground state of the $3d^5$ configuration in these energy diagrams have been excited to higher energy states using λ_{exc} = 405 nm (3.6 eV). Afterwards, these electrons undergo non-radiative decay to the $^4T_1(^4G)$ state and then a radiative-decay transition to the ground state ($^6A_1$).[25] Similarly, in the $3d^3$ configuration, free electrons in the $^4A_2(^4F)$ ground state are excited to higher energy states. These states are followed by non-radiative decay to the $^2E(^2G)$ state and then a radiative-decay transition to the $^4A_2(^4F)$ ground state. The PL spectra of samples containing $Zn_{0.9}Mn_{0.1}Te$ and $Zn_{0.2}Mn_{0.8}Te$ (Fig. 6 (A)) show an emission band centred at 715 nm (1.73 eV) that results from a spin-forbidden ligand transition (^2G) → $^4A_2$ (^4F) from Mn^{4+} ions in octahedral sites[12] (Fig. 6(B)).

The PL spectra of the samples containing $Zn_{0.995}Mn_{0.005}Te$, $Zn_{0.9}Mn_{0.1}Te$ and $Zn_{0.2}Mn_{0.8}Te$ NCs (Fig. 6(A)) show that relative intensities (I_{QDs}, I_{bulk}, I_{Eo} and $I_{Mn^{2+}}$ (Td)) decreased whereas $I_{Mn^{2+}}$(Oh) and $I_{Mn^{4+}}$(Oh) intensities increased as concentration increased. These reductions in relative intensity (I_{QDs}, I_{bulk} and I_{Eo}) that occur as concentration increased from x = 0.005 to x = 0.100

clearly confirm the substitutional incorporation of Mn^{2+} ions in $Zn_{1-x}Mn_xTe$ NCs. However, at high concentrations (x = 0.800), the E_{exc}, E_b and E_O emission bands practically disappear, resulting in near-zero $I_{QDs,}$ I_{bulk} and I_{Eo}. This proves that the nucleation rate for the formation of the $Zn_{1-x}Mn_xTe$ NCs decreased with increasing Mn concentration. This result is also confirmed by the OA spectra (Fig. 1), which show reductions in the intensity of the absorption band attributed to $Zn_{1-x}Mn_xTe$ NCs (QDs and bulk-like NCs). Decreases in I_{Mn}^{2+} (Td) and increases in I_{Mn}^{2+}(Oh) and I_{Mn}^{4+}(Oh) are attributed to structural changes that arise from the different occupations of manganese ions in the host network. Thus, it can be inferred that at low Mn concentrations (x ≤ 0.100), more Mn^{2+} ions were located in tetrahedral sites (Td). In other words, these ions were incorporated into ZnTe NCs at low concentrations (Figure 7 (A)), but formed MnO and MnO_2 NCs at high concentrations (x > 0.100) when emissions from Mn^{2+} and Mn^{4+} ions located in octahedral sites (Oh) predominated (Figure 7 (B)).

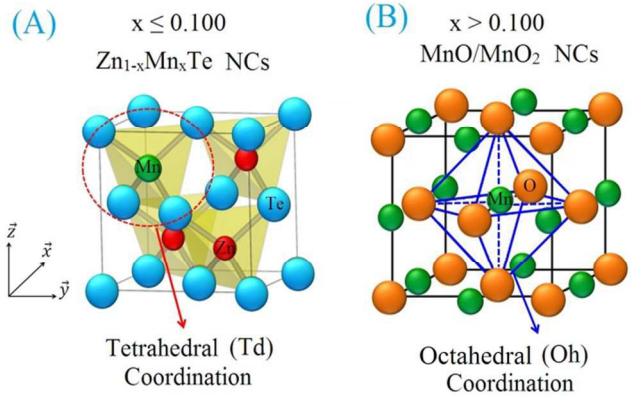

Figure 7. (A) Mn^{2+} ions located in tetrahedral sites (Td) of ZnTe NCs (concentration x < 0.100). (B) Mn^{2+} and Mn^{4+} located in octahedral sites (Oh) of MnO and MnO_2 NCs (concentration x ≥ 0.100).

According to CFT, the crystal field Δ of a tetrahedral site is lower than that of Mn^{2+} located in octahedral sites [$\Delta(T_d) \sim 0.5\Delta(O_h)$].[26] This significant change in the crystal field around the magnetic ion and consequently its local electron structure, produced the variations in optical energy transitions observed in the optical and emissions spectra.[27] Given this result, a redshift is expected in the PL spectra as magnetic ion doping increases. This is provides clear evidence that there are many more Mn^{2+} ions in tetrahedral sites (Td) within the ZB structure of the $Zn_{1-x}Mn_xTe$ NCs before reaching solubility limits (x > 0.100) and forming MnO NCs. It can also be said that some of these Mn^{2+} ions change from the 2+ oxidation state (Mn^{2+}) to the 4+ state (Mn^{4+}), thereby forming MnO_2 NCs. These MnO and MnO_2 NCs have local octahedral symmetry. The ability to tune the $^4T_1(^4G) \rightarrow {}^6A_1(^6S)$ emission energy of Mn^{2+} ions from orange (Td site) to near infrared (Oh site) and the ability to increase sample luminescence at higher concentrations are very interesting for applications in luminescent devices.

Conclusions

Manganese-doped ZnTe NCs ($Zn_{1-x}Mn_xTe$) were successfully grown in a glass matrix that was transparent to near UV, produced by the fusion method and subjected to appropriate thermal annealing. Tanabe-Sugano energy diagrams were used to study how increases in Mn concentration (from x = 0.000 to x = 0.800) modify the local crystal field of this transition metal. Therefore, we investigated the physical properties of our samples by optical absorption (OA), transmission electron microscopy (TEM), atomic/magnetic force microscopy (AFM/MFM) and photoluminescence (PL). OA and CFT provided strong evidence that Mn^{2+} ions were substitutionally incorporated into $Zn_{1-x}Mn_xTe$ NCs until reaching their solubility limit (concentration x = 0.100). At higher concentrations, the formation of MnO and MnO_2 NCs probably initiated in the PZABP glass system. This result was confirmed by TEM images that showed interplanar distances that correspond to $Zn_{1-x}Mn_xTe$ NCs at low concentrations (x ≤ 0.100) and $Zn_{1-x}Mn_xTe$, MnO and α-MnO_2 NCs at high concentrations (x > 0.100). AFM images showed that NC density on the surface of the glass matrix decreased as x-content increased. At high concentrations, MnO and MnO_2 NCs probably outnumbered $Zn_{1-x}Mn_xTe$ NC – a conclusion that was corroborated by OA and TEM. Magnetic phase images (MFM) revealed that samples with Mn^{2+} ions responded to magnetization from an MFM probe. This implies that Mn^{2+} ions were incorporated into the $Zn_{1-x}Mn_xTe$ NCs and gave rise to the DMS structure. The PL spectra not only confirmed the evidence shown by OA, CFT and TEM, but also showed that it was possible to tune the $^4T_1(^4G) \rightarrow {}^6A_1(^6S)$ emission energy from orange to near infrared as a function of concentration. This capability is very interesting for applications in luminescent devices.

Acknowledgements

We gratefully acknowledge financial support from the Brazilian Agencies: Conselho Nacional de Desenvolvimento Científico e Tecnológico-CNPq, Fundação de Amparo à Pesquisa do Estado de Minas Gerais-FAPEMIG, and Programa Nacional de Pós Doutorado da Coordenação de Aperfeiçoamento de Pessoal de Nível Superior (PNPD CAPES) – Instituto de Física (INFIS), Universidade Federal de Uberlândia (UFU). We are also grateful for use of the AFM/MFM Shimadzu at the INFIS – UFU.

Notes and references

[a]*Universidade Federal de Uberlândia, Instituto de Física, Laboratório de Novos Materiais Isolantes e Semicondutores (LNMIS), Uberlândia, Brazil. CEP: 38400-902; Tel: +55+34+3239-4190; *E-mail: assilva@doutorado.ufu.br (Dr. Alessandra S. Silva).*
[b]*Universidade Tecnológica Federal do Paraná, Engenharia de Materiais, CEP 86036-370, Londrina, Paraná, Brazil.*

DOI: 10.1039/b000000x/

1 T. Dietl, H. Ohno, *Rev. Mod. Phys.* 2014, **86**, 187–251.
2 S. A. Wolf, D. D. Awschalom, R. A. Buhrman, J. M. Daughton, S. von Molnar, M. L. Roukes, A. Y. Chtchelkanova, D. M. Treger, Spintronics: A Spin-Based Electronics Vision for the Future. *Science* 2001, **294**, 1488–1495.
3 P. Wojnar, E. Janik, L. T. Baczewski, S. Kret, E. Dynowska, T. Wojciechowski, J. Suffczynski, J. Papierska, P. Kossacki, G. Karczewski, J. Kossut, T. Wojtowicz, *Nano Lett.* 2012, **12**, 3404-3409.
4 K. Ando, *Appl. Phys. Lett.* 2003*,* **82**, 100-102.
5 G. Yang, G. Xu, B. Chen, S. Zou, R. Liu, H. Zhong, B. Zou, *Chemistry of Materials* 2013, **25**, 3260-3266.
6 D. A. Bussian, S. A. Crooker, M. Yin, M. Brynda, A. L. Efros, V. I. Klimov, *Nat. Mat.* 2008, **8**, 35-40.
7 Y. Ding, L. B. Liang, M. Li, D. F. He, L. Xu, P. Wang, X. F. *Nanscale Research Letters* 2011, **6**, 119.
8 R. Belauc, P. I. Archer, S. T. Ochsenbein, D. R. Gamelin, *Advanced Functional Materials* 2008, **18**, 3873-3891.
9 A. Nag, R. Cherian, P. Mahadevan, A. V. Gopal, A. Hazarika, A. Mohan, A. S. Vengurlekar, D. D. Sarma, *J. Phys. Chem C* 2010, **114**, 18323-18329.
10 N. O. Dantas, A. S. Silva, E. S. F. Neto, S. A. Lourenço, *Phys. Chem. Chem. Phys.* 2012, **14**, 3520-3529.
11 N. O. Dantas, A. S. Silva, S. W. Silva, P. C. Morais, M. A. Pereira-da-Silva, G. E. Marques, *Chem. Phys. Lett.* 2010, **500**, 46-48.
12 M. A. Noginov, G. B. Loutts, *J. Opt. Soc. Am. B* 1999, **16**, 3-11.
13 A. V. R. Kumar, C. S. Rao, N. N. Rao, V. R. Kumar, I.V. Kityk, *Journal of Non-Crystalline Solids* 2012, **358**, 1278–1286.
14 B. Henderson, G. F. Imbusch, *Clarendon Press Oxford* 1989, 48-76.
15 Y. W. Lin, W. J. Chen, J. Y. Lu, Y. H. Chang, C. T. Liang, Y. F. Chen, J. Y. Lu, *Nanoscale Research Letters* 2012, **7**, 401.
16 M. A. Ahmed, K. E. S. Rady, K. M. El-Shokrofy, A. A. Arais, M. S. Shams, *Materials Sciences and Applications* 2014, **5**, 932-942.
17 B. Liu, X. Hu, H. Xu, W. Luo, Y. Sun, Y. Huang, *Scientific Reports* 2014, **4**, 4229.
18 M. Wei, Y. Konishi, H. Zhou, H. Sugihara, H. Arakawa, *Nanotechnology* 2005, **16**, 245-249.
19 L. Zhao, B. Zhang, Q. Pang, S. Yang, X. Zhang, W. Ge, J. Wang, *Appl. Phys. Lett.* 2006, **89**, 092111.
20 A. S. Silva, A. Franco Jr., F. Pelegrini, N. O. Dantas, *Journal of Alloys and Compounds* 2015, 647, 637-643.
21 D. V. Korbutyak, N. D. Vakhnyak, D. I. Tsutsura, O. M. Pihur, R. M. Peleshchak, *Ukr. J. Phys.* 2007, **52**, 378-381.
22 Y.-M. Yu, S. Nam, K.-S. Lee, Y. D. Choi, O. Byungsung, *J. Appl. Phys.* 2001, **90**, 807-812.
23 M. H. Wan, P. S. Wong, R. Hussin, H. O. Lintang,; S. Endud, *Journal of Alloys and Compounds* 2014, **595**, 39–45.
24 L. Gacem, A. Artemenko, D. Ouadjaout, J. P. Chaminade, A. Garcia, M. Pollet, O. Viraphong, *Solid State Sci.* 2009, **11**, 1854.
25 J. L. Rao, C. R. Kesavulu, R. S. Muralidhara, R.V. Anavekar, R. P. S. Chakradhar, *J. Alloys Comp.* 2009, **486**, 46.
26 R. G. Burns, Mineralogical Applications of Crystal Field Theory. Second Edition ed.; Cambridge University Press: Cambridge, UK, 1993.
27 F. J. Torres, U. R. Rodriguez- Mendoza, V. Lavin, E. R. de Sola, J. Alarcon, *Journal of Non-Crystalline Solids* 2007, **353**, 44-46.